Turkish Journal of Civil Engineering, 2024 19-45, Paper 786, ***Research Article***

Debris Flow Impact on Rigid Walls: Protection by Tree Trunks

Pakhshan AHMADIAN[1*]
Umut TÜRKER[2]

ABSTRACT

To mitigate debris flow disasters, most of the previous research has focused, mostly through experimental methods, on placing different rigid barriers as structural prevention against debris flow to dissipate its energy. However, there has been less research on simulating the debris flow resistance on the tree trunk patches. In the present work, analytical and numerical simulation of the peak impact pressure of debris flow on a vertical rigid wall has been analysed under the protection of a patch of tree trunks. Along the debris flow path, tree trunks with identical diameters have been arranged in linear and rectilinear configurations. The mathematical analysis employs the Reynolds Transport Theorem, while the numerical simulations use the Reynolds-Averaged-Navier-Stokes equations. The numerical simulation results have depicted that the rectilinear configuration of tree trunks in each spot area is more effective than other configurations and increasing density of tree trunks within a given spot area is 50% more protective than the increasing the number of rows of the tree trunks. Additionally, this study estimates a new dynamic coefficient (α) as a function of the Froude number and devises a new expression for the drag force coefficient for different tree trunk configurations.

Keywords: Debris flow, rigid barriers, tree trunks, Reynolds transport theorem, Reynolds-averaged-Navier-Stokes.

1. INTRODUCTION

Based on the National Research Council (NRC) (Areas (1982)), the mud floods, mudflows, and debris flows have been classified as hyper-concentrated sediment flows. Based on the dominant shear stress from these three components, Julien and Leon (2000) offered a classification of hyper-concentrated sediment flows in debris flow in which dispersive stress

Note:
- This paper was received on July 11, 2023 and accepted for publication by the Editorial Board on June 11, 2024.
- Discussions on this paper will be accepted by January 31, 2025.
- https://doi.org/10.18400/tjce.1325755

1 Eastern Mediterranean University, Department of Civil Engineering, Famagusta, Turkish Republic of Northern Cyprus / pakhshan.ahmadian@cc.emu.edu.tr - https://orcid.org/0000-0002-3428-035X

2 Eastern Mediterranean University, Department of Civil Engineering, Famagusta, Turkish Republic of Northern Cyprus / umut.turker@emu.edu.tr - https://orcid.org/0000-0002-31647419

* Corresponding author

is dominant. Debris flow is the solid-liquid two-phase flow that consists of slurry or water containing silt, clay and sand (Thouret et al. (2020)). Since the kinetic energy of debris flow is very high, its interaction with engineering structures along their paths can be devastating (Armanini (1997)). Extreme impact force causes serious damage that can even end in societal disasters. Therefore, the determination of the debris flow impact force on any obstacle along their path should be taken as a priority (Yazid et al. (2017) and Mahnamfar et al. (2020)). There are several ways to carry out and calculate the debris flow impact forces. These can be categorized as analytic formulas, experimental studies at fields or flumes, or numerical analyses based on previous studies. Previously, several studies of debris flow impact forces have been conducted based on field measurements (e.g., Leonardi and Pirulli (2020) and Yan et al. (2023)) and scaled experiments (e.g., Scheidl et al. (2012); Cui et al. (2015); Armanini et al. (2019) and Song et al. (2021)). Debris flow impact forces have been defined as the combination of slurry and grain impact loading (Lei et al. (2018)). Moreover, slurry impact pressure studies can be classified into two groups: hydrostatic models and hydrodynamic models (Lichtenhahn (1973); Zanchetta et al. (2004)).

To mitigate the disasters, most of the previous researchers have focused on placing different dams as rigid barriers which were taken as structural prevention against debris flow disasters to trap the soiled materials. Also, the construction of a concrete baffle array is an alternative way to minimize the destructive effect of debris flow. In this kind of structure, the height, type and distance between each baffle play an essential role in mitigation purposes. In general, scientists prefer to perform numerical simulation or fieldwork to determine the performance of baffle structures (Ng et al. (2015); Bi et al. (2018); Wang et al. (2020); Yang et al. (2021); Deng et al. (2022); Kim and Yune (2022) and Kim et al. (2023)). Numerous studies have studied baffles constructed at slopes where granular flows were accelerated (Choi et al. (2015)) and at deposition zone where granular flows were decelerated (Wang et al. (2020)).

Like baffle array structure, a patch of trees can also contribute to reduce debris flow mobility and reducing the triggering capacity of the debris flow. The presence of the tree trunks increases the debris flow resistance, prevents debris flow from moving, supports the deposition of debris, and most importantly, reduces the maximum impact forces on structures (Fidej et al. (2015) and Bettella et al. (2018)). In addition, interest has recently been increasing in the study of tree trunks or vegetation in debris flow disasters to dissipate debris flow energy on their paths. The effect of trees on debris-flow deposits has been studied extensively in the past few years. Researchers have been studying how tree trunks (in cases of rigid vegetation) affect the flow patterns in rivers, streams, coastal dunes and floodplains (Mashud et al. (2011); Vargas-Luna et al. (2015); Türker et al. (2019) and Kumar et al. (2021)), but few studies investigated the effect of a patch of trees as a preventive measurement against debris flow disaster. The rigid vegetation or tree trunks exert drag forces against debris flow that can greatly reduce debris flow velocities near the bed (Liu et al. (2021)) and also can reduce suspended sediment transport and sediment erosion (Vargas-Luna et al. (2015) and Kang et al. (2022)). The majority of experimental and theoretical studies of cylinder arrays (representing vegetation canopies or tree trunk solid fraction) have been addressed for water flow. These research have consistently shown the effect of canopy density on the drag coefficient and water flow velocity (Tanino et al. (2008); Etminan et al. (2017); D'Ippolito et al. (2019); Chang et al. (2020); Mancheño et al. (2021) and Sohrabi et al. (2023)). Tree trunks increase flow resistance by exerting drag forces, as a result, the mean

debris flow velocity and bed shear stress were reduced so that the water levels become high. Additionally, the tree trunk forces the flow to move around, which changes the flow field around tree trunks (Nepf (2012) and Liu et al. (2016)). There is still an incomplete understanding of the morphologies of debris flow behavior, and fewer studies have addressed patches of tree structures and their interactions within debris flow material along with their travel distances.

The experimental analyses by considering the assumptions about the material concentration, particle size distribution and rheological parameters alone can be inaccurate in measuring the impact force of debris flows. A variety of factors might cause inaccuracies, including environmental conditions, human error during experiments, variations in the frequency of debris flows, and discrepancies in devices and testing methods. Therefore, making accurate numerical analysis and employing an analytic method can be effective ways to obtain accurate debris flow impact force. In the present work, an analytical investigation and a numerical evaluation were conducted to compare the behaviour of debris flow, its impact force and distribution when it encounters a rigid wall by comparing results from several previous large-scale and small-scale laboratory experiments. the amount of conservation of mass, momentum and energy that passes through the selected control volume was evaluated by the Reynolds Transport Theorem (RTT). The simulation results were analysed by FLOW-3D, a three-dimensional finite element model, that provides valuable insight into several physical flow processes. The Renormalized Group (RNG) based on k-epsilon model was used as a turbulence model. This model is the most precise, highly suitable and robust model for accurately simulating mass flow dynamics. To offer better coverage, it expands the capabilities of the standard k-epsilon model. Basically, the Navier-Stokes equations which describe the motion of fluids in three-dimensional space were solved and this gives the ability to measure the peak impact pressures on the rigid wall. The aim of this study is to determine the maximum impact pressure of debris flow over a rigid vertical wall, right after passing through different configurations of patches of tree trunks. For the development of effective measures, two different configurations were simulated. In one of the simulations the number of rows of tree trunks increased towards upstream, whereas, in the second configuration, the density of tree trunks increased within a predefined area.

2. METHODOLOGY

Debris flow is a function of Froude number (Fr), which is the ratio between the inertial and gravitational forces and was given as follows:

$$F_r^2 = \frac{u^2}{g\,H\cos\theta} = \frac{\rho u^2}{\rho g H\cos\theta} = \frac{\text{Inertial force}}{\text{Gravitational force}} \quad (1)$$

where u is debris flow velocity (m/s), g is the gravitational acceleration (m/s^2), H (h=H cosθ as depicted in Fig. 1) is the vertical flow depth (m), θ is the flume bed inclination.

Depending on the Fr the magnitude and the behaviour of debris flow changes. In this research, the numerical analysis is based on the experimental study performed by Cui et al. (2015) where the debris flow was examined under supercritical flow conditions; the Fr is always greater than 1.

The debris flow generally generates high kinetic energy named as the hydrodynamic impact force. This was initially studied by Hungr et al. (1984) and later by Armanini (1997), showing that the hydrodynamic impact force is proportional to both debris flow velocity and debris flow density, ρ. Hence the debris flow maximum impact pressure (P_{dmax}) equation was given as follows:

$$P_{dmax} = \alpha\rho\, u^2 \tag{2}$$

In which ρ is (kg/m3), and α is the empirical proportionality coefficient for hydrodynamic models that can be experimentally identified according to the type of debris flow. For instance, α =2.0 was suggested by Watanabe (1981) for laminar and fine aggregate debris flows, whereas values between 2.0 and 4.0 were measured by Egli (2005) for debris flows which mainly involve coarse aggregate. Values between 3 and 5 were reported after 70 field investigations of debris flow tests in China (Zhang (1993)).

Hübl et al. (2009) used dimensional analysis and proposed a method for estimating debris flow P_{dmax} against protecting structure expressed as:

$$\frac{P_{dmax}}{\rho u^2} = a\, F_r^b \tag{3}$$

Where the parameters of (a) and (b) are empirical factors and their values are between 4.9 to 5.62 and -1.66 to -1.29, respectively (Hübl et al. (2009)).

2.1. Momentum Conservation Law

2.1.1. Reynolds Transport Theorem

Based on the definitions given by Takahashi (1979); Chu et al. (1995) and Mangeney et al. (2010), a change in the momentum of the debris flow originates the impact impulse pressure on a rigid wall. The total forces per unit width that act on the control volume on the sloping bed in the x direction is:

$$F_{Tx} = \int_{L_x}^{L+L_x} \left[\bar{\rho} g\, \bar{h}\, sin\,\theta \; - k\bar{\rho} g\, \bar{h} \frac{d(h)}{dx} - \bar{\rho} g\; \bar{h} \tan\varphi\right] dx \tag{4}$$

Where φ represents the friction angle of the material, $\bar{\rho}$ represents depth-averaged debris flow density , $\bar{h}$ represents the average depth along the x-direction that is $\bar{h} = z_{top} - z_{bed}$, L represents the control volume length and L_x is the length of the flume upstream of the control volume. The angle of inclination of the bed slope was represented by θ. The first term is gravitational force which represents body force due to gravity that acts on the control volume, the second and third terms represent external force components, normal and tangential on the control volume (Fig. 1).

Solving Reynolds Transport Theorem to obtain the momentum flux model that is appropriate to define incoming momentum flux which flushes to downslope one obtains:

$$\bar{\rho}u_{in}^2\, h_{in} + \bar{\rho}g\, \bar{h}L\, sin\,\theta\ - k\bar{\rho}g\, \bar{h}L\frac{d(h)}{dx} - \bar{\rho}g\, \bar{h}L\tan\varphi = \bar{\rho}u_{out}^2\, h_{out} \quad (5)$$

where $\bar{\rho}u_{in}^2\, h_{in}$, ($\dot{M}_{in}$), and $\bar{\rho}u_{out}^2\, h_{out}$, ($\dot{M}_{out}$) are debris incoming and outgoing momentum flux per unit width, respectively, $h_{in} = H_{in}cos\theta$, $h_{out} = H_{out}cos\theta$, $\bar{\rho}g\, \bar{h}L\, sin\,\theta$ is the gravitational force (F_g) component per unit width, $k\bar{\rho}g\, hL\frac{d(h)}{dx}$ is the longitudinal pressure force (F_p) per unit width due to longitudinal variations in depth h, and $\bar{\rho}g\, \bar{h}\,L\tan\varphi$ is the basal friction force (F_{bs}) per unit width as illustrated in Fig. 1.

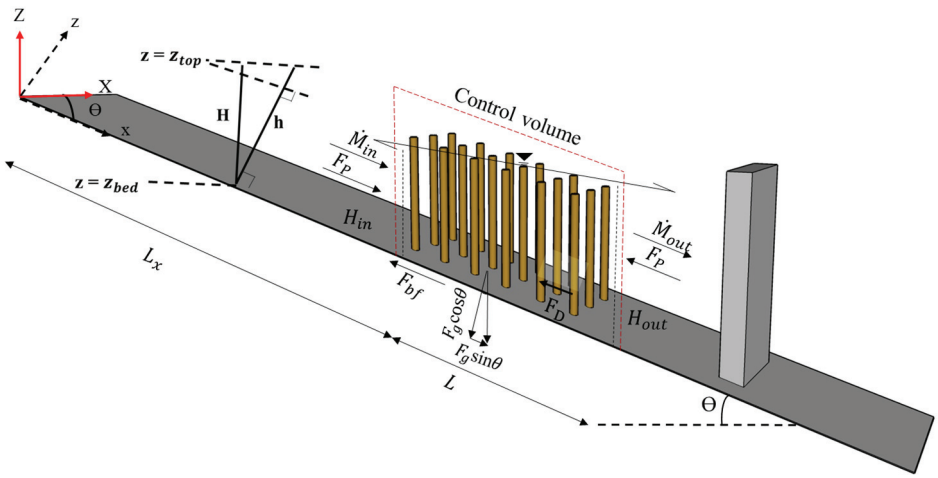

Fig 1 - Sketch of the flume geometry and the total forces that act on the control volume attributed to the tree trunk patches arrangement at an inclined bed with the angle of (θ).

3. MODEL PROGRESS

3.1. Drag Force

Nowadays, referring to the more specific reference of the field of rigid vegetation, rigid tree trunks have often been demonstrated by circular cylinders made of various materials either in experimental or simulation models. Due to the influence of the tree trunks against debris flow, the drag forces were exerted and can be expressed as $\sum_{i=1}^{N} F_D$ where N is the number of the tree trunks per unit plan area.

Formally, the depth integration of drag force for a single vertical cylinder with diameter d, from z_{bed} to z_{top} can be expressed as follows:

$$F_D = \int_{zbed}^{ztop} \frac{1}{2} C_D\, \bar{\rho}u^2 d\, \cos\theta\, dz \quad (6)$$

In which C_D is the drag coefficient and d being the tree trunk diameter.

By inserting Eq.6 into Eq.5, the momentum conservation equation applied along flow direction given in Fig.1 can be rewritten as:

$$\bar{\rho}u_{in}^2 h_{in} + \bar{\rho}g\,\bar{h}\,L\sin\theta - k\bar{\rho}g\,\bar{\mathrm{h}}L\frac{\mathrm{d(h)}}{dx} - \bar{\rho}g\,\bar{\mathrm{h}}L\tan\varphi - \frac{1}{2}NC_D\,\bar{\rho}\bar{\mathrm{h}}u^2 = \bar{\rho}u_{out}^2 h_{out} \quad (7)$$

3.2. Tree Trunk Patches Methods

Several studies have been conducted on the interaction between flow and rigid vegetation in the past (e.g., Liu et al. (2016) and D'Ippolito et al. (2021)), but a few studies have been done on the effect of drag exerted from various vegetation densities on debris flow (e.g., Liu et al. (2021)). Here, the tree trunk simulation analyses are based on two different scenarios. In one of the simulations, the density of tree trunks (λ) increased within a predefined area (Fig. 2), and in the second configuration, the vegetated length parameters (∅) (the number of rows of tree trunks) increased towards upstream (Fig. 3).

A geometric similarity ratio value of 1:50 was used for the tree trunk diameter in the simulation. The cylinder with a 1 cm diameter and 14 cm in length was used in the simulated flow (Cost (1979)). Tree trunk density without canopy was presented by gradually increasing the number of individual rigid tree trunk elements in the measuring plane area, in two different linear and rectilinear arrays (A1, A2, A3, A4, A5 and A6), Fig. 2. In this group model two significant parameters, λ and solid volume fraction (ψ), have been examined. Referring to emergent rigid vegetation for cylindrical elements with a constant diameter (d) of past experimental studies (Valyrakis et al. (2021); Wilson et al. (2003) and Nepf (1999)), and based on the frontal area of the individual rigid elements per unit volume, the λ can be defined as the ratio of the projected rigid tree trunks plan area to the total volume:

$$\lambda = \frac{\mathrm{dh}}{\mathrm{s_i^2 h}} = \frac{\mathrm{d}}{\mathrm{s_i^2}} \quad (8)$$

where s_i represents the distance between adjacent individual tree trunk elements. The ψ is the ratio of the areal coverage of the tree trunk elements to the portion of measuring area covered by tree trunk elements previously defined by Türker et al. (2006), and expressed as:

$$\psi = \mathrm{N}\,\frac{\pi \mathrm{d}^2}{4\Delta\mathrm{X}\,\Delta\mathrm{Z}} \quad (9)$$

where ΔX is the horizontal distance, ΔZ is the vertical distance in measuring the plane area and N is the number of tree trunks in the area of concern. Two scenarios were proposed for determining the P_{dmax} applied by debris flow on vertical walls. The first scenario covers six different configurations in which linear and rectilinear patches of tree trunks were examined. The tree trunk densities and ψ ranging from λ = 1.3 m^{-1}, for the linear arrangement model A1, to λ = 44.4 m^{-1}, and for the rectilinear arrangement defined as configuration A6, (Table 1).

Table 1 - Plan view of cylinder tree trunks arrangement in simulation model

Model group A						
	Tree trunk arrangement	Horizontal distance on measuring plane ΔX (cm)	Vertical distance on measuring plane ΔZ (cm)	Tree trunk distance s_i (cm)	Solid volume fraction (ψ) %	Tree trunk density λ (m^{-1})
A1	Linear	10	8	10	1	1.3
A2	Rectilinear	10	8	6	1.96	2.8
A3	Linear	10	8	5	3.9	4
A4	Rectilinear	10	8	3	7.8	11.1
A5	Linear	10	8	2.5	15.7	16
A6	Rectilinear	10	8	1.5	31.4	44.4
Model group B						
		Tree trunks spacing perpendicular to debris flow direction ΔX (cm)	Tree trunks spacing parallel to debris flow direction ΔZ (cm)	Tree trunks diameter d (cm)	Number of rows N_r	Vegetated length parameter $\emptyset$
B1	Linear	4	5	1	1	0.04
B2	Linear	4	5	1	3	0.12
B3	Linear	4	5	1	5	0.2
B4	Linear	4	5	1	8	0.31
B5	Linear	4	5	1	12	0.47
B6	Linear	4	5	1	17	0.67

The second scenario has been examined with six different configurations in which the number of rows used for the tree trunks increased towards the upstream side of the flume. The first configuration is run with one row of tree trunks (B1) and then the number of rows increased to 3, 5, 8, 12 and 17 in the following configurations (Fig. 3.); spacing between each tree trunk was adjusted to ΔX =4 cm in the orthogonal direction to the flume direction and ΔZ =5 cm along the flume directions.

The dimensionless $\emptyset$ (Türker et al. (2019)) was obtained by the ratio of the volume of a single vegetation element in a unit area to the total volume of the unit area. The dimensionless $\emptyset$ varied between 0.04 and 0.67 as shown in Table 1. The $\emptyset$, based on its definition, was calculated as given in Eq 10.

$$\emptyset = N_r \frac{\frac{\pi}{4} d^2 h}{\Delta x \, \Delta z \, h} = N_r \frac{\pi d^2}{4 \, \Delta x \, \Delta z} \tag{10}$$

Where N_r is the row number of tree trunks and h represents the height of the tree trunk.

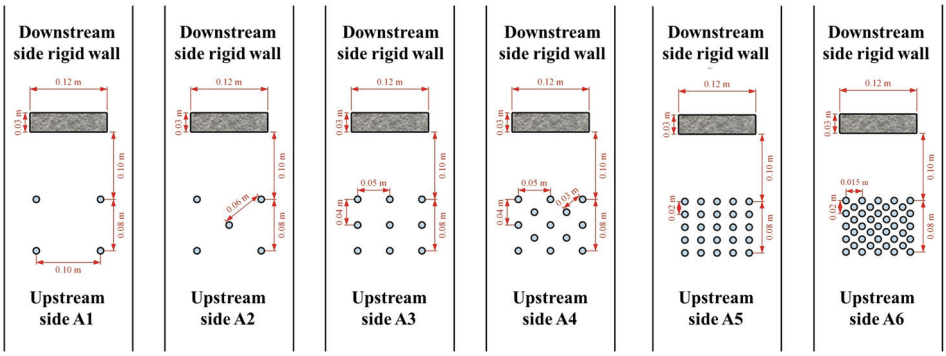

Fig 2 - The top view of the six different linear and rectilinear patches of tree trunk arrangements for model group A (A1, A2, A3, A4, A5 and A6).

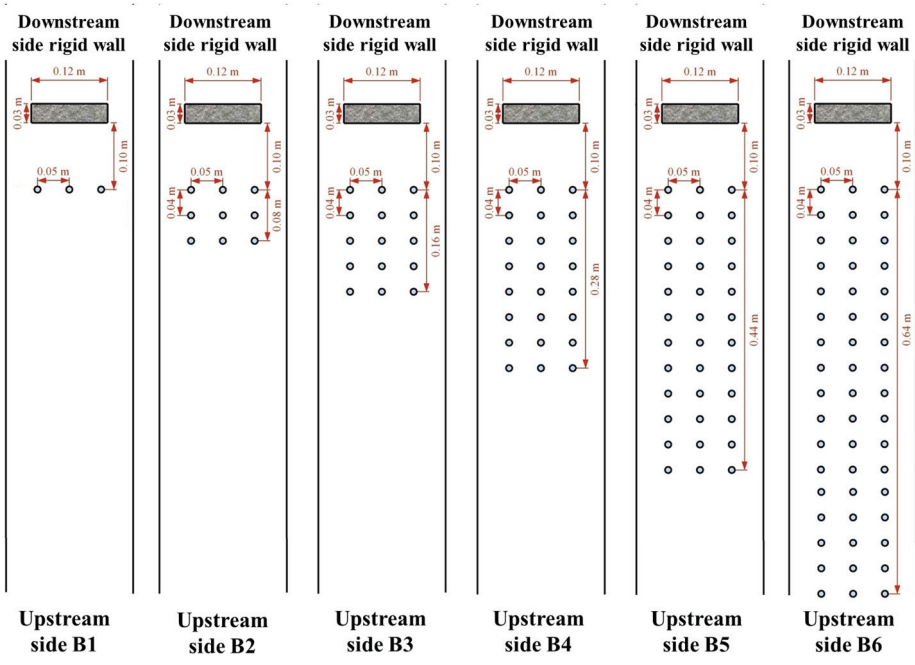

Fig 3 - The top view of the six different linear patches of tree trunk arrangements for model group B (B1, B2, B3, B4, B5 and B6).

4. MODEL SETUPS

The simulation results were performed by FLOW-3D, a three-dimensional finite element model. Continuity and momentum equations together with the finite volume method were used to solve the RANS equations.

4.1. Particle Size Distribution

According to data extracted from Cui et al. (2015), the materials that were used as input data for the model contained 2.9% clay, 5.1% silt, 37% sand, and 55% gravel. The ρ is 2074 (kg/m³) with a water concentration of 0.35 and a total volumetric concentration of 0.63. Consequently, the volumetric concentrations for clay, silt, sand, and gravel are 39.1 (kg/m³), 68.7 (kg/m³), 498.8 (kg/m³), and 741.4 (kg/m³), respectively. The cumulative percent passing of grain size, represented in Fig. 4, was employed as input data for defining debris flow particle size. As shown in the graph, the maximum particle size is 20 mm. To achieve the same material contents of the different grain size diameters that align with experimental data, four different gravel contents of 6%, 5%, 29%, and 15%, with diameters of 16 mm, 12 mm, 8 mm, and 3 mm were applied in the model respectively. Additionally, four different sand contents of 11%, 9%, 14%, and 3%, with diameters of 1.75 mm, 0.9 mm, 0.375 mm, and 0.11 mm were assigned respectively. Furthermore, for the silt and clay contents, percentages of 5.1% and 2.9% with diameters of 0.04 mm and 0.002 mm were respectively applied in the model.

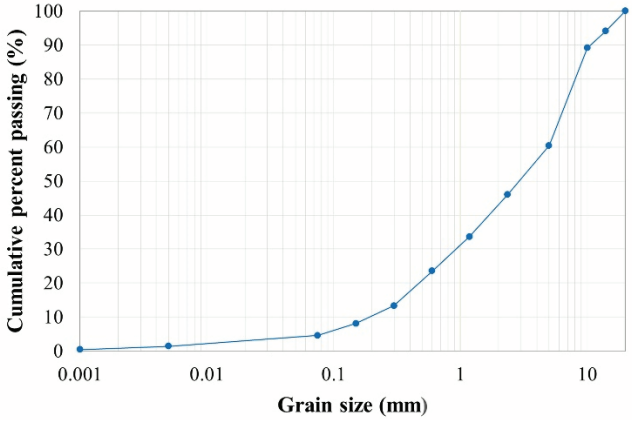

Fig 4 - Debris flow cumulative grain size distribution.

4.2. The Geometry and Boundary Condition of Numerical Analysis

In analysing debris flow impact force, crucial factors were selected with reference to previous studies. The simulated flume is 300 cm long and 20 cm wide with an inclination angle of 15° which was shown in Fig. 5. The 3 cm thick wall was placed at the end of the flume. The height of the wall is 25 cm, and its width is 12 cm. The debris material was flushed down by a gate with a 20x20 cm^2 area, placed at 50 cm from the top of the flume as a flow inlet. To measure the debris flow impact pressure, 18 measurement points (historical probes) were applied and positioned on the wall at different vertical heights: 1.5 cm, 4.5 cm, 7.5 cm, 10.5 cm, 13.5 cm, and 16.5 cm from the bottom of the rigid wall.

A wall boundary type was assigned to X_{min}, Y_{min}, Y_{max} and Z_{min} since there is no outflow in that region. On the other hand, outlet flow was applied at X_{max}, and a symmetry boundary type was assigned at Z_{max} as illustrated in Fig. 5.

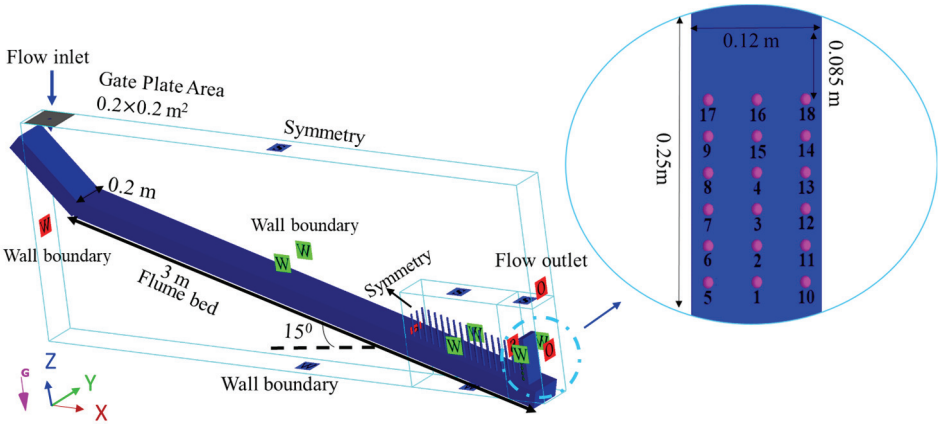

Fig 5 - Debris flow simulation model Geometry with various boundary condition types and 18 measurement points (historical probes) on the rigid wall.

As part of setting up the model, all material contents were applied in the fluid initialization, and material diameters were specified in the physics of the model as the sediments scour window. In the mass momentum source window, the debris flow geometry and properties were performed, including details such as the shape (a square with dimensions of 20 x 20 cm²), flow direction (oriented along the z-axis), and rotation (a 180-degree rotation in the y-direction). This configuration is depicted in Fig. 5, which represents the flow geometry at the inlet flow. To achieve the same debris flow discharge as the experimental results, the flow rate was programmed as 0.11 (m^3/s) between the time (0 - 2), 0.05 (m^3/s) between the time (2 – 2.5), 0.01 (m^3/s) between the time (2.5 – 3.1), 0.005 (m^3/s) between the time (3.1 – 4), 0.001 (m^3/s) between the time (4 - 5), 0.0001 (m^3/s) between the time (5 - 8) and zero for time 8 (sec). The debris flow characteristics and input data used in the simulation model are listed in Table 2.

The cartesian meshes were generated using the nested multi-block grid mesh in FLOW-3D to minimise the model memory usage and runtime. Several meshes were tested in the simulation model to ensure that the numerical solution remains consistent and does not significantly change with different grid settings. Due to dealing with elements of different sizes, both uniform and non-uniform Cartesian mesh sizes were defined in the geometry. A uniform Cartesian mesh cell size of 0.005 m was used as finite meshes for the entire area. To improve mesh size precision for the tree trunk area and rigid wall, two different non-uniform block meshes were employed as illustrated in the Fig. 6.

In block (a), the cell counts 100 and 200 were applied in both y and z directions for all group models A and B, respectively. However, due to different configurations in the x direction for group models A and B, the cell counts of 200 were allocated to the B6 model, the longest tree truck rows, in the x direction which indicated the average mesh sizes of 0.002 m. To provide uniform precision for all group models A and B, a ratio of 308 cell counts per meter was applied. Furthermore, in block (b), cell counts of 100 were assigned in the x, y, and z directions for all group models. The total number of real cells for all mesh blocks is 11474000. To increase the usefullness of results in FLOW-3D, the size ratio between the

adjacent cells should be close to unity as much as possible and must not exceed 1.25. Moreover, aspect ratios of the cells should also approximate unity as much as possible, and not exceed 3.0 because cell aspect ratios exceeding 3.0 can cause pressure iteration problems. Furthermore, all degrees of freedom for cells at all the sides (x, y and z) and bottom were fixed as shown as mesh planes in Fig. 6.

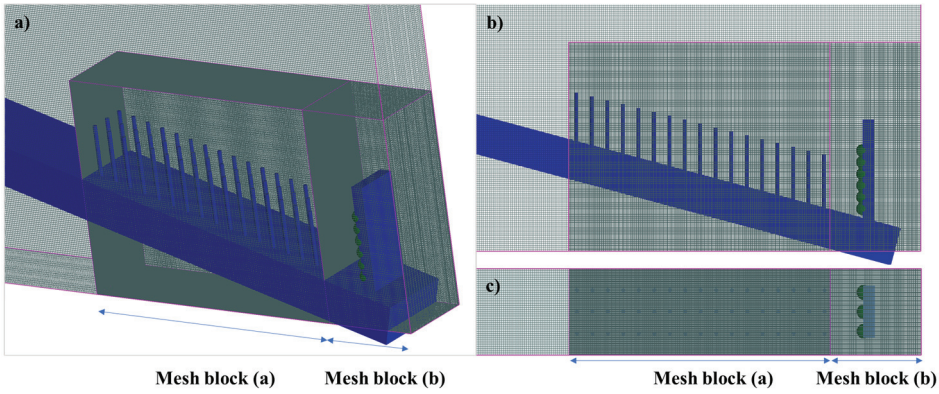

Fig 6 - Computational mesh grid in the control volume of the simulated model with two different adding mesh block (a) and (b): section a) 3D view, section b) side view and section c) top view.

Table 2 - Debris flow simulation input variable

Parameters	***Value***
Specific gravity (Gs)	2.65
Flume inclination angle (degrees)	15
Average grain diameter d_{50} (m)	0.0027
Dynamic Viscosity (Pa s)	0.096
Yield stress (Pa)	30.32
Fluid viscosity (kg/m/s)	*0.001*
Debris flow fluid density (kg/m^3)	*2074*
Friction angle (degrees)	32
Water concentration	0.35
Sediment volume concentration	0.63
Total debris flow volume (m^3)	0.23

5. VALIDATION OF THE TOTAL IMPACT FORCES

The debris flow simulation analysis validation conducted with and without sediment particle (clean water) distribution using the experimental results of Cui et al. (2015). Based on their

experiment, the length of the flume is 300 cm, the width is 20 cm, and the inclination angle is 15°. Five impact measurement points (historical probes) S1 to S5 were located at the end of the flume. These points were placed on the wall at 1.5 cm, 4.5 cm, 7.5 cm, 10.5 cm, and 13.5 cm vertical depths from the bottom of the wall. In their experiments, the flow impact pressure processes can be considered into three stages. First, there is a strong impact at the head of the debris flow, followed by a steady impact along the body, and finally, there is a sliding flow at the tail. Due to the lower impact pressure in the debris flow tail, only the initial two steps were considered by them as the impact pressures. Consequently, the impact pressure measured at 10.5 cm and 13.5 cm heights were excluded from their calculations.

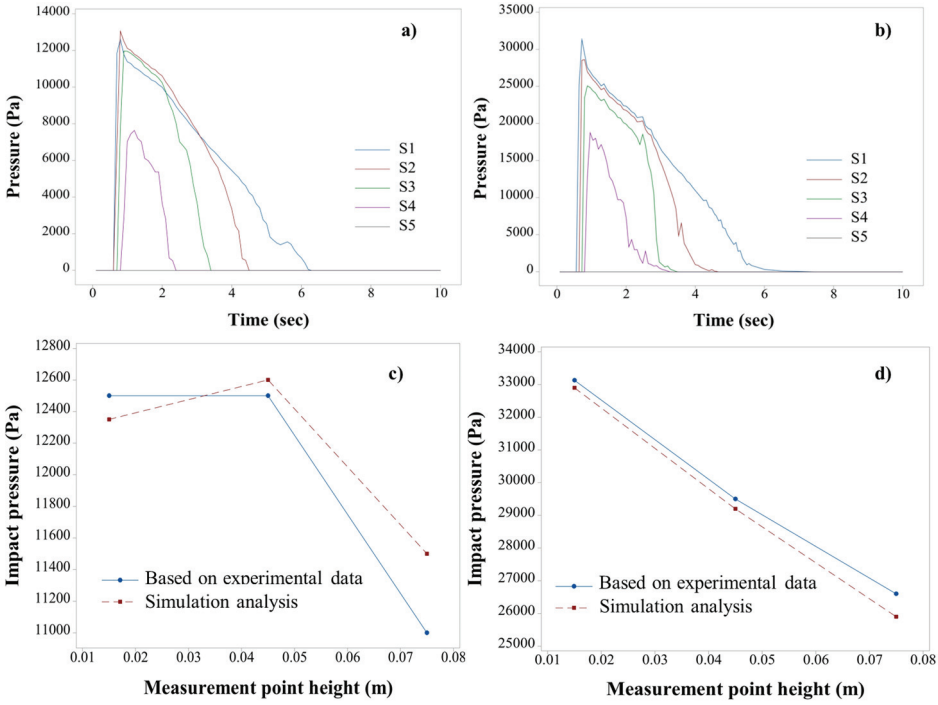

Fig 7 - Impact pressure determination for different measurement points (1.5 cm, 4.5 cm, and 7.5 cm above the flume bed) that placed at different height, (a) clean water, (b) debris flow and validation of experimental data based on simulation analysis for (c) Clean water and (d) Debris flow.

Based on the simulation and experimental results, both clean water and debris flow impact pressures do not reach point S5 in terms of height. The velocity of the clean water is estimated at 4.9 m/s, Fr is 5.2 and the P_{dmax} is 12.6 kPa (Fig. 7-a). Using the input parameters provided in Table 2 for water with sediment particles, the respected values were u of 4.1 m/s, Fr of 3.8, and P_{dmax} of 32.9 kPa (Fig.7-b). The impact pressure process at the first measurement point S1 was sustained for about 6 seconds and other points was sustained for 3-4 seconds. Fig. 7-c and -d show the comparison between experimental data and simulation results in three different measurement point heights; 1.5 cm, 4.5 cm, and 7.5 cm from the flume bed.

In clean water, the percentage error of the simulated analyses is less than 2% for the first and second heights, and below 5% for the third height compared to the experimental results. Similarly, in the debris flow the percentage error of the simulated analyses at each height is less than 2% of experimental results. As a result, the MSE is 0.09 for clean water and 0.13 for debris flow. Therefore, the findings are in good agreement with the experimental observations.

The analytical results obtained from Eq.4 were validated by using experimental data from Cui et al. (2015). In their experiment, they conducted a total of 27 tests, with a range of Fr variation between 2.5 and 5.9. Subsequently, these results were compared with 155 tests of previous data with Fr between 0.5 and 10.8 by Hübl and Holzinger (2003); Tiberghien et al. (2007) and Scheidl et al. (2012) and field experiment analyses by Costa (1984) and Zhang and Yuan (1985). In this study, subcritical flow data (Fr<1) have not been included in comparison. The result of the regression hydrodynamic model derived by Cui et al. (2015) was expressed in Eq.11 and was given in Fig. 8:

$$\frac{P_{dmax}}{\rho\, u^2} = 5.3\, Fr^{-1.5} \tag{11}$$

The impact pressure analysis data from Cui et al. (2015) were inserted into Eq. 4 and the results were plotted on the power line with a regression error square (R^2) of 0.95 to show that the results matched with the previous studies. Based on these ranges the dimensionless empirical coefficient, α is analytically calculated to be in the range of 0.4 and 1.86.

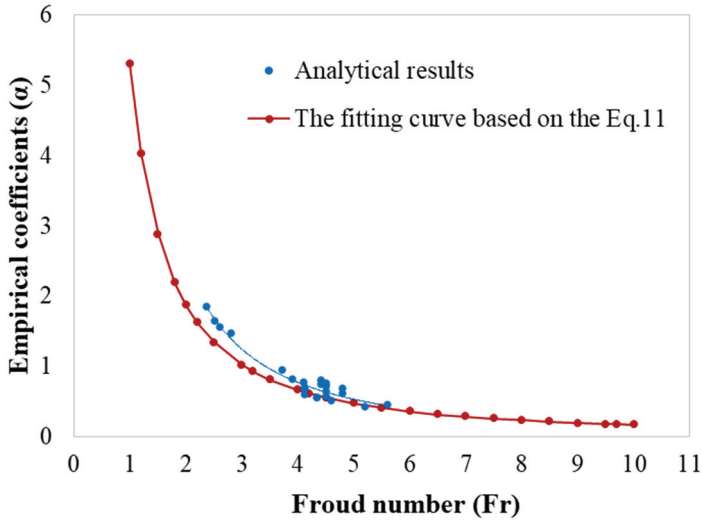

Fig 8 - Relationship between empirical coefficients and the Fr based on Analytical and experimental results

5.1. Impact Pressure Simulation

Twelve model tests were performed with different tree trunk arrays in both linear and rectilinear directions. All forces per unit meter were measured with specified density, tree trunk diameters, and distances. The results are shown in Table 3. The momentum flux leaving the control volume of the vegetated area generates pressure on the vertical wall. Eighteen measuring points (S1 to S18) have been used to assess impact pressure on the wall. Each point was arranged to have a 3 cm vertical and 4 cm horizontal distance from each other. Variation of impact pressures at S1, S2, S3, S4, S15 and S16, that were placed at different depths for both A4 and B5 models, as a function of time are depicted in Fig. 9 and Fig. 10. It can be noted that, with the increase of tree trunks against the debris flow path, the duration of the rigid wall impact pressure also increases. For instance, approximately 9 to 10 seconds were estimated to be sustained for A4 and 8 to 9 seconds for B5 as indicated in Fig. 9 and 10. The arrival time of peak impact pressures based on the effect of tree trunks was shown in Table 3, where peak impact pressure arrival times were changed from 0.76 to 1.2 seconds for group model A and from 0.76 to 0.9 seconds for group model B.

Table 3 - Numerical results for both group models A and B.

Group models A										
Solid volume fraction (ψ) %	Peak Impact arriving Time (sec)	Depth H_{out} (cm)	Velocity u (m/s)	Froude number	$\dot{M}_{in}$ (kN/m)	F_D (kN/m)	F_g (kN/m)	F_p kN/m)	F_{bs} (kN/m)	$\dot{M}_{out}$ (kN/m)
1	0.76	14	4.6	3.93	47.8	2.2	0.60	0.62	1.45	44.1
1.96	0.8	16.5	3.9	3.06	47.8	20.8	7.10	0.74	1.71	31.6
3.9	0.8	15.2	4.2	3.48	47.8	8.7	0.68	0.70	1.64	37.4
7.8	1	18.9	3.4	2.49	47.8	29.1	8.15	0.84	1.97	24
15.7	1	17.2	3.7	2.87	47.8	23.6	7.41	0.77	1.79	29
31.4	1.2	25.4	2.5	1.61	47.8	41.5	10.90	1.13	2.63	13.4
Group models B										
Vegetated length parameter, ø	Peak Impact Arriving Time (sec)	Depth H_{out} (cm)	Velocity u (m/s)	Froude number	$\dot{M}_{in}$ (kN/m)	F_D (kN/m)	F_g (kN/m)	F_p kN/m)	F_{bs} (kN/m)	$\dot{M}_{out}$ (kN/m)
0.04	0.76	14.7	4.4	3.6	47.8	6.5	0.70	0.73	1.69	39.6
0.12	0.8	15.2	4.2	3.5	47.8	8.7	0.68	0.70	1.64	37.4
0.2	0.9	16.1	4.0	3.2	47.8	12.9	0.72	0.75	1.74	33.1
0.31	0.9	17	3.8	2.9	47.8	16.2	0.76	0.79	1.84	29.7
0.47	0.9	17.1	3.8	2.9	47.8	16.4	0.77	0.79	1.85	29.5
0.67	0.9	17.1	3.8	2.9	47.8	16.4	0.77	0.79	1.85	29.5

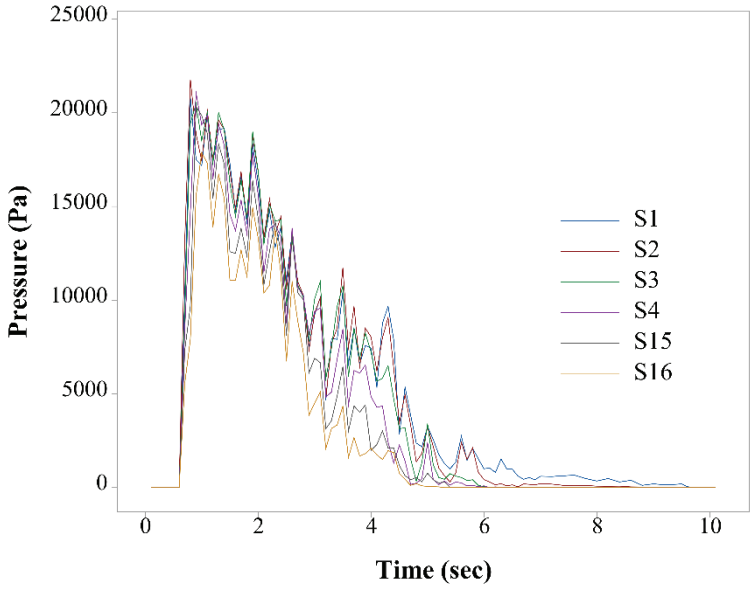

Fig 9 - Debris flow impact Pressures at measurement points (S1, S2, S3, S4, S15 and S16) were placed at different depths for model A4.

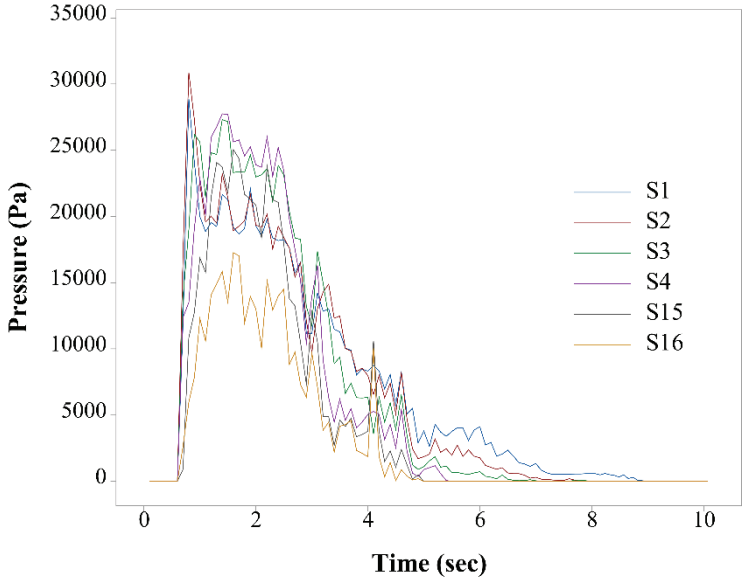

Fig 10 - Debris flow impact Pressures at measurement points (S1, S2, S3, S4, S15 and S16) were placed at different depths for model B5.

Fig. 11 and 12 show the front view impact pressure distribution along the rigid wall models A and B. It can be seen that for group model A (linear and rectilinear), P_{dmax} was concentrated between 4.5 to 10.5 cm above the floor. As ψ increased, independent of linear or rectilinear configurations of tree trunks, the effect of impact pressure decreased. When the maximum impact pressures at A1 are compared with the max impact pressures at A6, a reduction of 67.3%, 69.5% and, 70% in maximum pressures were observed at S4, S3, and S2, respectively. Another important observation is the increase in the depth of flow in parallel to the increase in ψ. Due to the velocity retarding effect (drag force effect) of the tree trunks, there is a reduction in u from 4.6 to 2.5 (m/sec) in the flow direction. Based on the principles of continuity, a decrease in velocity increases the flow area, which in turn increases the depth of the debris flow; depth increased from 14 cm to 25 cm. Consequently, the reduction in the velocity did not change the regime of the flow and the supercritical flow properties dominate the flow. However, as is seen in Fig. 11, a considerable increase in maximum impact pressures at the top of the wall was observed due to the rise in the debris flow depth. The retarding effect of tree trunks on the occurrence time of peak impact pressures was given in Fig. 11 indicates a 58% shift in the occurrence time of peak impact pressures.

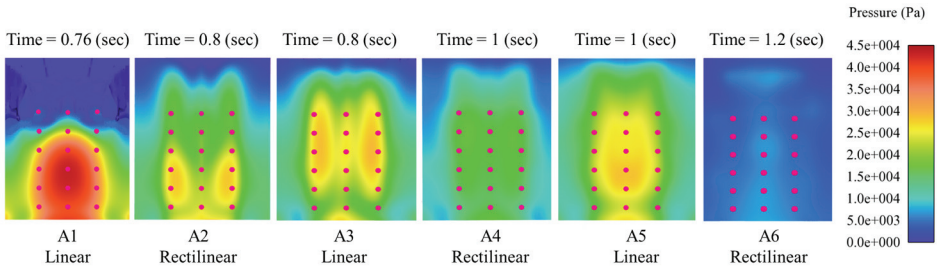

Fig 11 - The pressure distributions in the 18 measurement points on the rigid wall for group models A with various λ (1.3, 2.8, 4, 11.1, 16 and 44.4, m^{-1}) and ψ (1, 1.96, 3.9, 7.8, 15.7 and 31.4, %).

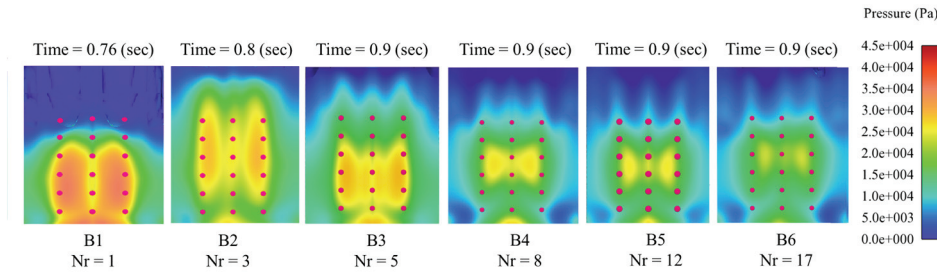

Fig 12 - The Pressure distributions in the 18 measurement points on the rigid wall for group models B with various Ø, (0.04, 0.12, 0.2, 0.31, 0.47 and 0.67).

The simulation for model B configurations clearly depicted the effect of drag on the debris flow. The in-line ordered trunks providing an easy path for debris flow to reach the wall caused maximum impact pressures. On the other hand, as the ∅ increased, the pressure dropped in the projection of tree trunks. Simulated peak pressures on the wall were 39 kPa in model B1 and 29 kPa in model B6. Approximately, a 34% reduction in peak impact pressure is not as good as the results achieved in Model A simulations. A significant reduction in debris flow velocity is not observed as in the case of model A simulations. As the ∅ increases from 0.04 to 0.67, a slight decrease, from 4.4 m/s to 3.8 m/s, in u was observed. Meanwhile, the flow depth increased from 15 cm to 17 cm. Consequently, the necessary time required to observe the occurrence of peak impact pressures on the wall did not vary much (Fig. 12).

5.2. Normalized Drag Coefficient

There are several studies that define the drag force and coefficient based on various assumptions. Some of them ignore the dominant effect of the Reynolds number (e.g. Riazi and Türker (2019)) while some assume that the drag force is linearly changing with flow velocity (e.g. Türker and Valyrakis (2021)). Implementing the drag force concept on linearly and randomly distributed trees based on using a quadratic drag law it was concluded that the variation in drag force increases as the λ increases. For the analyses of C_D along an individual tree trunk, the drag force equation (Eq. 5) can be given as:

$$C_D = \frac{2F_D}{\bar{\rho}u^2 dH} \tag{12}$$

in which H is debris flow depth. Based on the data given in (Table 3), under the assumption that debris flow velocity, debris flow density and tree trunk area are constant at the entrance of control volume, the magnitude of C_D will vary as the tree trunk ψ and ∅ change. Therefore, the C_D increases as the number of tree trunks increases. In other words, C_D in a normalized form should take into consideration the amount of tree trunks. Hence, based on this observation, for the assessment of the normalized drag coefficient (C_{DN}) associated with the debris flow resistance due to rigid tree trunks the following expression was proposed:

$$C_{DN} = C_D \times \eta \tag{13}$$

where η is the mean value of the correlation drag coefficient for each different λ.

There are several different methods to define the tree trunk C_D for the group tree trunk model in which C_D is not the same as a single tree trunk and has typically been modified to increase with λ (Nepf (1999); Tanino and Nepf (2008); Kothyari et al. (2009); Stoesser et al. (2009)).

The drag force was equally distributed within the control volume among the different tree trunks to examine drag coefficients.

The graph in Fig. 13 shows the variation of C_{DN} with various row numbers, Nr. The values of η and C_{DN} for the six different group model B are in the range of about 1.0-2.5 and 0.2-1.2 (Table 4). The graph exhibits that C_{DN} increases with an increase in row numbers and

eventually assumes a maximum value. This could be due to the possibility that the debris flow became fully developed after a certain length of vegetation array.

The nonlinear regression equation describing the change in C_{DN} with respect to the number of rows was given in Eq. 14 with a mean square error (MSE) of 0.03 and the standard error of the regression (S) of 0.18. Equation 14 was derived to describe the C_{DN} valid for the simulation performed in this study.

$$C_{DN} = 1.2 - 1.44\exp(-0.24N_r) \quad (14)$$

Table 4 - Results of C_D, η and C_{DN} with different ψ number of rows

	C_D	η	C_{DN}
(ψ) %		**Group model A**	
1	0.07	1.0	0.1
1.96	0.62	9.4	5.9
3.9	0.44	6.6	2.9
7.8	0.87	13.2	11.5
15.7	0.71	10.7	7.6
31.4	`1.24	18.8	23.3
N_r		**Group model B**	
1	0.20	1.00	0.2
3	0.26	1.32	0.3
5	0.39	1.96	0.8
8	0.49	2.46	1.2
12	0.49	2.49	1.2
17	0.49	2.49	1.2

The values of η for linear group model A are in the range of about 1 to 10.7 and for rectilinear group model A are in the range of 9.4 to 18.8 (Table 4). The graph in Fig. 14 shows the variation of C_{DN} with various ψ for linear and rectilinear tree trunk models. The C_{DN} increases with increasing the number of tree trunks within a predefined area in both linear and rectilinear models. As illustrated in Fig. 14, the increase in rectilinear models is more pronounced compared to the linear model.

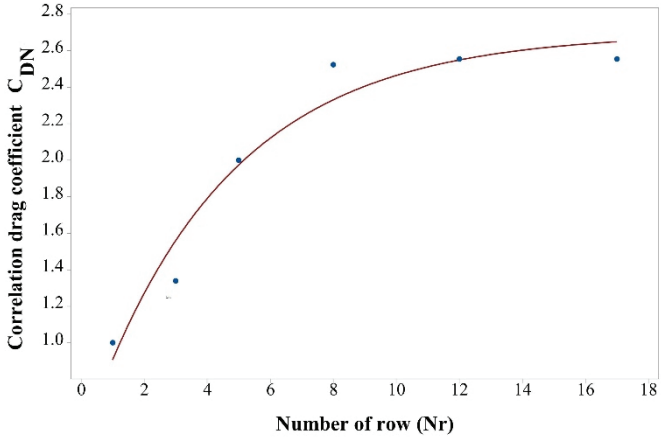

Fig 13 - Variation of C_{DN} with various row numbers (Nr) for group model B.

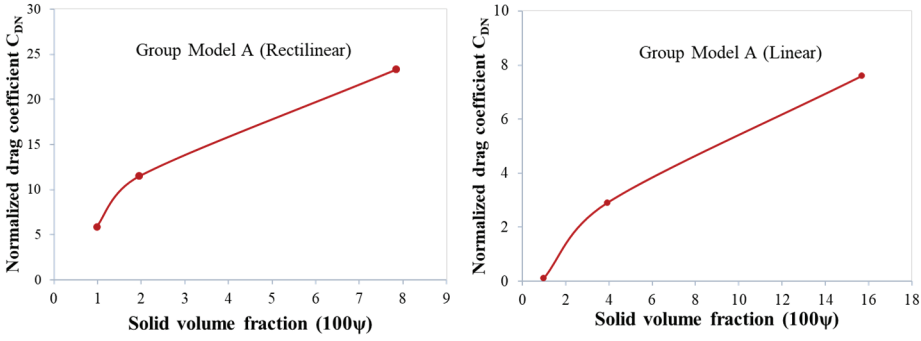

Fig 14 - Variation of C_{DN} with various ψ for group model A (Linear and Rectilinear).

To assess the influence of tree trunks on C_{DN} more completely, the normalized regression equation was defined as a function of the Fr and ψ for group model A and N_r for group model B as follows:

$$C_{DN} = 39.69 - 0.33\ln(100\psi)^{0.002} - 30.38\ln(Fr)^{0.85} \quad (15)$$

$$C_{DN} = 7.45 - 0.12\ln(N_r)^{0.72} - 5.63\ln(Fr)^{0.99} \quad (16)$$

These equations imply that drag coefficients have a weak dependence on tree trunks ψ fractions and row numbers as compared Fr. The agreement between the the proposed equations and estimated C_{DN} values is satisfactory as shown in Fig. 15.

Several factors affect the hydrodynamic empirical coefficient; the characteristics of a basin, the features and properties of debris flows, and intensity of rainfall. Previously obtained debris flow experimental results show that the hydrodynamic empirical coefficient can be

estimated within the range of (2.8–4.4) (Lichtenhahn (1973)), (2.5–7.5) (Scotton and Deganutti (1997)) and (0.45-2.2), (Armanini (1997)).

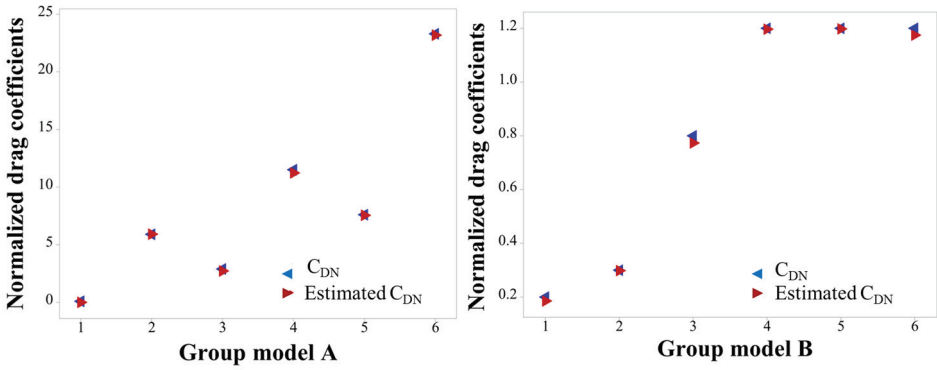

Fig 15 - Comparison between the C_{DN} and the estimated C_{DN} based on the results which obtained from Eq. 15 and Eq. 16 for both group models A and B.

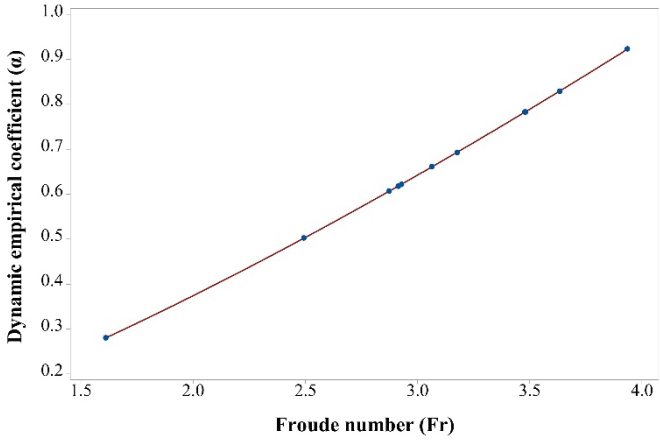

Fig 16 - Relationship between the Fr and dynamic empirical coefficient (α)

The magnitude of hydrodynamic empirical coefficient, α, has been assessed experimentally by using a flume to evaluate the impact force of debris flow as explained above. Fig. 16 depicts the variation of the dynamic empirical coefficient, α, as a function of Fr. In the present work, the presence of tree trunks increases the resistance forces, and the empirical coefficient was estimated to be in the range of (0.28–0.92) for the range of Fr varying between 1.6 and 3.9. Referring to Eq. 3, by having a new finding of P_{dmax}, the following hydrodynamic model with mean square error (MSE) 0.0004 and the standard error of the regression (S) 0.006 were introduced as:

$$\alpha = 0.15F_r^{1.33} \tag{17}$$

6. DISCUSSION

Based on the analytical and numerical calculations, the ratio between pressure forces and inertia forces which is the dynamic empirical coefficient, α, has been modified for the cases where the protection of patch of tree trunks was present (Eq. 17). In this study, the values of a and b were determined as 0.15 and 1.33, respectively. As a result, the relationship between Fr and dynamic empirical coefficient follows a power law. However, under normal conditions (without any mitigation techniques) which have been studied previously, the value of a ranges from 4.9 to 5.62 and the value of b ranges from -1.66 to -1.29, indicating that the Fr and α are inversely proportional (Hübl et al. (2009) and Cui et al. (2015)).

This result reveals the effect of the patch of tree trunks on reducing the magnitude of inertia forces. Such reduction reduces the Fr, therefore, to reduce α, since inertia force ρu^2 is decreasing, P_{dmax} should also be decreased. This can only be satisfied if the constant b is positive, 1.33. This result suggests that in the case of protective mitigation, the magnitude of b should be positive.

Implementation of the baffle array is a similar artificial technique to mitigate debris flow disasters. Studies conducted by Bi et al. (2018), Wang et al. (2020) and Yang et al. (2021) demonstrated that the baffle row numbers, column spacing, and row spacing all have significant influences on the baffle energy dissipation. According to their results, increasing the number of baffle rows and spacing increases baffles energy dissipation capacity which indicates the reduction in the debris flow velocity. Also, Ng et al. (2015) investigated the effects of baffle spacing and row numbers and their experimental results depicted reduced u by increasing the number of rows of baffles. By increasing from one row to three rows, u was reduced by 57 %. In this study, a reduction in the debris flow velocity is also observed. However, the reduction is not as high as in baffle cases but is up to 47% in the A type models and 21% for the B type models. Such a result indicates that natural mitigation methods might not be as successful as artificial ones but still can reduce risks generated by debris flow. In addition, Zhang et al. (2021) worked out the effect of baffle arrays at the acceleration stage of the granular flow and according to their results, u was reduced by 78.82%.

Many studies have recently investigated the C_D exerted by cylindrical arrays in the case of water flow. These findings examined flow patterns similar to the results investigated for debris flow in this study. Studies conducted by Tanino et al. (2008); Etminan et al. (2017); Chang et al. (2020); Mancheño et al. (2021) and Sohrabi et al. (2023) showed that by increasing ψ, the C_D increases and consequently the drag force increases. Also, D'Ippolito et al. (2019) investigated that by increasing λ, C_D increases by 50 %. Since the debris flow density is higher than the water flow, the results of this study indicated the C_D increases by 90% and 59% in both grope models A and B, respectively.

At the same time, some studies were made to examine the variation of exerted drag force with the effect of blockage and sheltering (Li and Shen (1973); Schoneboom et al. (2011); Etminan et al. (2017) and Liu et al. (2020)). From the perspective of the blockage and sheltering effect, the finding of this study have also been validated by those results. Etminan et al. (2017) and Liu et al. (2020) found that the blockage effect with high vegetation densities had a greater impact on reducing C_D than sheltering effects in rectilinear configurations. However, in the linear configuration with the constant blockage ratio, the sheltering effect

showed more strength, which was evidenced by parallel findings regarding the blockage and sheltering effects observed in this study.

In this study, the rectilinear configuration of tree trunks in each spot area was more effective than other configurations. When the maximum impact pressures at A1 were compared with the maximum impact pressures at A6, a reduction of 67.3%, 69.5% and, 70% in maximum pressures were observed at S4, S3, and S2, respectively and a 34 % reduction in peak impact pressure for model B.

For group model A (linear and rectilinear), the P_{dmax} concentration appears in a different region of the wall. The variation of impact pressure concentration is similar to the damaged regions of the wall. There is a relatively high impact pressure region over the wall from S1 to S4 in A1 (linear model). Increasing the tree trunk arrangements from A2 to A6 gradually reduces the effect of P_{dmax} and expands its effect to a large area, therefore, the damaged regions were altered.

Future research should focus on studying the debris flow velocity field, with a particular concentration on the debris flow surfaces and developing methods to determine the velocity field around patches of tree trunks.

7. CONCLUSION

The study focused on the effect of debris flow peak impact pressure on a vertical wall which has been analysed under the protection of a patch of tree trunks. Both numerical simulation and the analytical model have been applied and validated.

Based on research findings, the following conclusions were drawn:

1. The numerical simulation results depicted that increasing λ within a given spot area is 50% more protective than the increase in the number of rows of tree trunks.
2. An increase in λ is also effective in retarding the occurrence period of the peak flows in model A around 58%. For model B, since only the number of rows is increased, it has changed by 18.4% up to the B3 model (five tree trunk rows); its increase has not affected on occurrence period of the peak for the other models at all. Thus, based on the results of the eight, twelve and seventeen rows of tree trunks investigation, the design basis for the five rows of tree trunks was suggested for model B.
3. The P_{dmax} is concentrated between 4.5 and 10.5 cm above the floor.
4. Based on the analytical calculations the C_D has been developed as a function of Fr and the new dynamic empirical coefficient α has been modified based on the analytical results.
5. The C_D was defined as a function of Ø and ψ. Accordingly, the presence of patches of tree trunks plays a significant role in reducing debris flow impact pressure and thus minimizing the hazard risks. It is clear that accurate numerical analysis and analytic methods can be effective in obtaining accurate debris flow impact force simulations. This study can be improved and developed by using different sediment and water concentrations to test the P_{dmax} on the walls. In addition, this study can be improved by using an experimental system, such as the physical model of the

prototype, and converting the findings to values likely to be encountered in nature in future studies.

References

[1] Areas NRC (US). C on M for PM (1982) Selecting a methodology for delineating mudslide hazard areas for the National Flood Insurance Program. National Academies

[2] Armanini A (1997) On the dynamic impact of debris flows. In: Recent developments on debris flows. Springer, pp 208–226

[3] Armanini A, Rossi G, Larcher M (2019) Dynamic impact of a water and sediments surge against a rigid wall. J Hydraul Res

[4] Bagnold RA (1954) Experiments on a gravity-free dispersion of large solid spheres in a Newtonian fluid under shear. Proc R Soc London Ser A Math Phys Sci 225:49–63

[5] Bettella F, Michelini T, D'Agostino V, Bischetti GB (2018) The ability of tree stems to intercept debris flows in forested fan areas: A laboratory modelling study. J Agric Eng 49:42–51

[6] Bi Y, Du Y, He S, et al (2018) Numerical analysis of effect of baffle configuration on impact force exerted from rock avalanches. Landslides 15:1029–1043

[7] Chang W-Y, Constantinescu G, Tsai W-F (2020) Effect of array submergence on flow and coherent structures through and around a circular array of rigid vertical cylinders. Phys Fluids 32

[8] Choi CE, Ng CWW, Law RPH, et al (2015) Computational investigation of baffle configuration on impedance of channelized debris flow. Can Geotech J 52:182–197

[9] Chu T, Hill G, McClung DM, et al (1995) Experiments on granular flows to predict avalanche runup. Can Geotech J 32:285–295

[10] Cost ND (1979) Multiresource inventories: a technique for measuring volumes in standing trees. Southeastern Forest Experiment Station

[11] Costa JE (1984) Physical geomorphology of debris flows. In 'Developments and applications of geomorphology'.(Eds JE Costa, PJ Fleisher) pp. 268–317

[12] Cui P, Zeng C, Lei Y (2015) Experimental analysis on the impact force of viscous debris flow. Earth Surf Process Landforms 40:1644–1655

[13] D'Ippolito A, Calomino F, Alfonsi G, Lauria A (2021) Flow resistance in open channel due to vegetation at reach scale: A review. Water 13:116

[14] D'Ippolito A, Lauria A, Alfonsi G, Calomino F (2019) Investigation of flow resistance exerted by rigid emergent vegetation in open channel. Acta Geophys 67:971–986

[15] Mangeney, A., Roche, O., Hungr, O., Mangold, N., Faccanoni, G., & Lucas, A. (2010). Erosion and mobility in granular collapse over sloping beds. Journal of Geophysical Research: Earth Surface, 115(F3)

[16] Egli T (2005) Wegleitung Objektschutz gegen gravitative naturgefahren. VKF

[17] Etminan V, Lowe RJ, Ghisalberti M (2017) A new model for predicting the drag exerted by vegetation canopies. Water Resour Res 53:3179–3196

[18] Fidej G, Mikoš M, Rugani T, et al (2015) Assessment of the protective function of forests against debris flows in a gorge of the Slovenian Alps. iForest-Biogeosciences For 8:73

[19] Hübl J, Holzinger G (2003) Development of design basis for crest open structures for debris flow management in torrents: miniaturized tests for the efficiency estimation of debris flow breakers. WLS Rep 50

[20] Hübl J, Suda J, Proske D, et al (2009) Debris flow impact estimation. In: Proceedings of the 11th international symposium on water management and hydraulic engineering, Ohrid, Macedonia. pp 1–5

[21] Hungr O, Morgan GC, Kellerhals R (1984) Quantitative analysis of debris torrent hazards for design of remedial measures. Can Geotech J 21:663–677

[22] Iverson RM, George DL, Logan M (2016) Debris flow runup on vertical barriers and adverse slopes. J Geophys Res Earth Surf 121:2333–2357

[23] Iverson RM, Ouyang C (2015) Entrainment of bed material by Earth-surface mass flows: Review and reformulation of depth-integrated theory. Rev Geophys 53:27-58

[24] Julien PY, Leon C (2000) Mud floods, mudflows and debris flows. Classification, rheology and structural design. Jornadas Investig JIFI

[25] Kang T, Jang C-L, Kimura I, Lee N (2022) Numerical Simulation of Debris Flow and Driftwood with Entrainment of Sediment. Water 14:3673

[26] Kim B-J, Choi CE, Yune C-Y (2023) Multi-scale flume investigation of the influence of cylindrical baffles on the mobility of landslide debris. Eng Geol 314:107012

[27] Kim B-J, Yune C-Y (2022) Flume investigation of cylindrical baffles on landslide debris energy dissipation. Landslides 19:3043–3060

[28] Kim SJ, Stoesser T (2011) Closure modeling and direct simulation of vegetation drag in flow through emergent vegetation. Water Resour Res 47(10)

[29] Kothyari UC, Hayashi K, Hashimoto H (2009) Drag coefficient of unsubmerged rigid vegetation stems in open channel flows. J Hydraul Res 47:691–699

[30] Kumar r, Singh nk (2021) Three dimensional flow over elliptic cylinders arrays in octagonal arrangement. J Therm Eng 7:2031–2040

[31] Lei Y, Cui P, Zeng C, Guo Y (2018) An empirical mode decomposition-based signal process method for two-phase debris flow impact. Landslides 15:297–307

[32] Leonardi A, Pirulli M (2020) Analysis of the load exerted by debris flows on filter barriers: Comparison between numerical results and field measurements. Comput Geotech 118:103311

[33] Li R-M, Shen HW (1973) Effect of tall vegetations on flow and sediment. J Hydraul Div 99:793–814

[34] Lichtenhahn C (1973) Berechnung von sperren in beton und eisenbeton. Mitt Forstl Bundes Versuchsanst Wein

[35] Liu C, Nepf H (2016) Sediment deposition within and around a finite patch of model vegetation over a range of channel velocity. Water Resour Res 52:600–612

[36] Liu M-Y, Huai W-X, Yang Z-H, Zeng Y-H (2020) A genetic programming-based model for drag coefficient of emergent vegetation in open channel flows. Adv Water Resour 140:103582

[37] Liu W, Yang Z, He S (2021) Modeling the landslide-generated debris flow from formation to propagation and run-out by considering the effect of vegetation. Landslides 18:43–58

[38] Mahnamfar F, Abdollahzadehmoradi Y, Ağiralioğlu N (2020) Flood risk analysis of residential areas at downstream side of Elmali Dam. Acad Platf J Nat Hazards Disaster Manag 1:49–58

[39] Malvern LE (1969) Introduction to the Mechanics of a Continuous Medium

[40] Mancheño AG, Jansen W, Uijttewaal WSJ, et al (2021) Wave transmission and drag coefficients through dense cylinder arrays: Implications for designing structures for mangrove restoration. Ecol Eng 165:106231

[41] Mangeney, A., Roche, O., Hungr, O., Mangold, N., Faccanoni, G., & Lucas, A. (2010). Erosion and mobility in granular collapse over sloping beds. Journal of Geophysical Research: Earth Surface, 115(F3)

[42] Mashud M, Al-Bari A, Kader MG (2011) Experimental investigation of drag force reduction mechanism for flow around a circular cylinder. Int J Eng Appl Sci 3:69–75

[43] Nepf HM (2012) Hydrodynamics of vegetated channels. J Hydraul Res 50:262–279

[44] Nepf HM (1999) Drag, turbulence, and diffusion in flow through emergent vegetation. Water Resour Res 35:479–489

[45] Ng CWW, Choi CE, Song D, et al (2015) Physical modeling of baffles influence on landslide debris mobility. Landslides 12:1–18

[46] Riazi A, Türker U (2019) The drag coefficient and settling velocity of natural sediment particles. Comput Part Mech 6:427–437

[47] Scheidl C, Chiari M, Mullegger M, Proske D (2012) Estimation of debris-flow impact forces using a small scale modelling approach. In: 12th Congress Interpraevent

[48] Schoneboom T, Aberle J, Dittrich A (2011) Spatial variability, mean drag forces, and drag coefficients in an array of rigid cylinders. Exp methods Hydraul Res 255–265

[49] Scotton P, Deganutti AM (1997) Phreatic line and dynamic impact in laboratory debris flow experiments. In: Debris-flow hazards mitigation: mechanics, prediction, and assessment. ASCE, pp 777–786

[50] Sohrabi S, Afzalimehr H, Singh VP (2023) Estimation of drag coefficient of emergent and submerged vegetation patches with various densities and arrangements in open channel flow. ISH J Hydraul Eng 29:297–307

[51] Song D, Chen X, Zhou GGD, et al (2021) Impact dynamics of debris flow against rigid obstacle in laboratory experiments. Eng Geol 291:106211

[52] Stoesser T, Salvador GP, Rodi W, Diplas P (2009) Large eddy simulation of turbulent flow through submerged vegetation. Transp porous media 78:347–365

[53] Takahashi T (1979) Study of the deposition of debris flows (1)-deposition due to abrupt change of bed slope-. Ann Disaster Prev Res Inst Kyoto Univ 22:315–328

[54] Tanino Y, Nepf HM (2008) Laboratory investigation of mean drag in a random array of rigid, emergent cylinders. J Hydraul Eng 134:34–41

[55] Thouret J-C, Antoine S, Magill C, Ollier C (2020) Lahars and debris flows: Characteristics and impacts. Earth-Science Rev 201:103003

[56] Tiberghien D, Laigle D, Naaim M, et al (2007) Experimental investigations of interaction between mudflow and an obstacle. Debris-flow hazards Mitig Mech Predict assessment, Millpress, Rotterdam

[57] Valyrakis, M., Liu, D., Turker, U., & Yagci, O. (2021). The role of increasing riverbank vegetation density on flow dynamics across an asymmetrical channel. Environmental Fluid Mechanics, 21, 643-666

[58] Türker U, Valyrakis M (2021) Hydraulic jump on rough beds: conceptual modeling and experimental validation. Water Supply 21:1423–1437

[59] Türker U, Yagci O, Kabdasli MS (2019) Impact of nearshore vegetation on coastal dune erosion: assessment through laboratory experiments. Environ Earth Sci 78:1–14

[60] Türker U, Yagci O, Kabdaşlı MS (2006) Analysis of coastal damage of a beach profile under the protection of emergent vegetation. Ocean Eng 33:810–828

[61] Vargas-Luna A, Crosato A, Uijttewaal WSJ (2015) Effects of vegetation on flow and sediment transport: comparative analyses and validation of predicting models. Earth Surf Process Landforms 40:157–176

[62] Wang D, Li Q, Bi Y, He S (2020) Effects of new baffles system under the impact of rock avalanches. Eng Geol 264:105261

[63] Watanabe M (1981) Investigation and analysis of volcanic mud flows in mt sakurajima, japan

[64] Wilson C, Stoesser T, Bates PD, Pinzen AB (2003) Open channel flow through different forms of submerged flexible vegetation. J Hydraul Eng 129:847–853

[65] Yan Y, Tang H, Hu K, et al (2023) Deriving Debris-Flow Dynamics From Real-Time Impact-Force Measurements. J Geophys Res Earth Surf 128:e2022JF006715

[66] Yang E, Bui HH, Nguyen GD, et al (2021) Numerical investigation of the mechanism of granular flow impact on rigid control structures. Acta Geotech 16:2505–2527

[67] Yazid AS, Adnan TFFT, Abdullah AA, et al (2017) Flood risk mitigation: Pressing issues and challenges. Int Rev Manag Mark 7:157–163

[68] Zanchetta G, Sulpizio R, Pareschi MT, et al (2004) Characteristics of May 5–6, 1998 volcaniclastic debris flows in the Sarno area (Campania, southern Italy): relationships to structural damage and hazard zonation. J Volcanol Geotherm Res 133:377–393

[69] Zhang B, Huang Y, Liu J (2021) Micro-mechanism and efficiency of baffle structure in deceleration of granular flows. Acta Geotech 16:3667–3688

[70] Zhang S (1993) A comprehensive approach to the observation and prevention of debris flows in China. Nat Hazards 7:1–23

[71] Zhang S, Yuan J (1985) Impact force of debris flow and its detection. Mem Lanzhou Inst Glaciol Cryopedology, Chinese Acad Sci Beijing Sci Press 269–274